Methods of data fusion of satellite imagery

Abstract

Many remote sensing applications require higher temporal resolution than can be captured by a single Landsat-class satellite. One solution to this problem is to use images from different sensors and combine them in a coherent product. However, this method requires different stages of processing to match the spatial resolution, the spectral characteristics, and the projection of the images, so that the fusion product can be treated as coming from a single sensor. In this review, different approaches to the fusion problem are presented and their respective advantages and shortcomings are highlighted.

Introduction

The advances in satellite imagery have created many opportunities for remotely sensed land monitoring applications. However, in many cases, more frequent observations than can be obtained from a single Landsat-like satellite are required or would greatly improve the quality of the results. The need for denser time series has been documented and would improve agriculture management (Claverie et al., 2012; S. Gao et al., 2013; Ma et al., 2013; Sibanda et al., 2015; Skakun et al., 2017; Whitcraft et al., 2015), monitoring of land cover changes (Hansen & Loveland, 2012), monitoring of forest and phenology (DeVries et al., 2015; Melaas et al., 2013; Vrieling et al., 2017; Zhu et al., 2012), flood risk management and disaster response (Hölbling et al., 2020; Skakun et al., 2014).

One approach to improve temporal resolution would be to increase the number of satellites in a single fleet as is offered by Planet Labs, however, due to the small size of the satellite and low-cost sensor, the spectral quality is not on par with larger satellites (Oriani et al., 2021). Another more opportunistic approach is to use data from different sensors and merge it into a single product of improved temporal resolution. However, images coming from different sensors will have different characteristics and thus need to be harmonized in a coherent product.

Landsat 8 (soon Landsat 9) and Sentinel-2 satellites offer similar resolution and spectral bands characteristics and therefore are good candidates for a fused product. The Landsat mission started in the 1970s and offers the longest-running continuous program of satellite imagery of the earth's land area (Loveland & Dwyer, 2012). The Landsat 8 mission started in 2013 and is a collaboration between NASA and the USGS. The satellite is equipped with two sensors, the Operational Land Imager (OLI) and the Thermal InfraRed Sensor (TIRS). It orbits sun-synchronously and offers a revisit interval of 16 days at the equator. The Sentinel-2 mission is operated by the European Space Agency and is currently composed of a constellation of two identical satellites phased 180 degrees from each other on the same sun-synchronous orbit. This allows a revisit cycle to be performed in 5 days at the equator. The satellites carry a single multi-spectral instrument that has similar spectral bands to Landsat 8 with a better spatial resolution. The spectral characteristics of Landsat 8 and Sentinel-2 are presented in Table 1. As we can see, the two satellites share many bands at similar resolutions, hence making them ideal candidates for a fused product.

The ideal fused product could be defined as follows (Claverie et al., 2018):

- Gridded to the same resolution, map projection, and spatial extent
- Atmospherically corrected to surface reflectance and cloud masked using a common radiative transfer algorithm calibrated for each product
- Normalized to a common NADIR view geometry to correct for the varying fly-over times
- Adjusted to represent the response from common spectral band-pass

Table 1: Spectral characteristics of Landsat 8 and Sentinel-2 (Claverie et al., 2018)

	Landsat 8	Sentinel-2
Ultra blue	443nm (30m)	443nm (60m)
Visible	482nm, 561nm, 655nm (30m)	490nm, 560nm, 665nm (10m)
Red edge	-	705 nm, 740 nm, 783 nm (20 m)
NIR	865nm (30m)	842nm (10m), 865nm (20m)
SWIR	1609nm, 2201nm (30m)	1610 nm, 2190 nm (20 m)
Cirrus	1373nm (30m)	1375 nm (60 m)
Water Vapor	-	945 nm (60 m)
Thermal	10.9μm, 12μm (100m)	-

These characteristics would allow users to treat the fused product as if it came from a single sensor without further corrections specific to one sensor. Moreover, the fusion of Landsat 8 and Sentinel-2 would greatly improve the temporal density of the resulting product. Using all three sensors, the global mean and median revisit interval at the equator decreases to 2.9 and 5.7 days respectively. This greatly improves the chances of capturing a cloudless image (Li & Chen, 2020; Li & Roy, 2017).

One problem arising from the fusion of different sensors is their differences in spatial resolution. Two approaches to combine the images are presented in this review. This first consists of upscaling the high-resolution product to match the low-resolution one. This ensures a higher certainty in the resulting images but discards potentially precious high frequencies spatial patterns that are captured by the higher resolution sensor. This approach is used in the Harmonized Landsat and Sentinel-2 surface reflectance data set (Claverie et al., 2018). The other approach consists of downscaling the lower resolution image, and thus preserves the information present in the high-resolution product. This can be done with multiple-point statistics methods like direct sampling (Oriani et al., 2021) which uses a training image to recreate high-resolution spatial pattern in the low-resolution image; kriging methods like ATPRK (Q. Wang et al., 2017) that uses temporally close high-resolution images of the same scene as covariates to downscale the low-resolution image; deep-learning-based methods like the convolutional neural network ESRCNN (Shao et al., 2019) that can use a flexible number of collocated high-resolution images to produce a super-resolved image, or GAN-based models (Chen et al., 2021) that only need image pairs for the training phase but can then downscale images without any reference image, allowing the downscaling of the Landsat archive for example. These five articles will be presented in this review.

Methods of data-fusion

The Harmonized Landsat and Sentinel-2 surface reflectance data set (Claverie et al., 2018)

The first method presented in this review has been developed at NASA by Claverie et al. (2018). It is based on the fusion of Sentinel-2 L1C and Landsat 8 L1T products. Sentinel-2 L1C is a radiometrically corrected top of the atmosphere (TOA) reflectance product that is orthorectified in WGS84 projection and grided in tiles of 110x110km (Ranghetti et al., 2020). Landsat-8 L1T images are also radiometrically corrected TOA reflectance and orthorectified in WGS84 projections, but they are gridded in tiles of 190x180km (U.S. Geological Survey, 2016). Although both products are radiometrically corrected, the resulting images are not consistent with each other.

The HLS dataset consists of three different products and is summarized in Table 2. The goal is to provide a dataset that offers a better temporal resolution than each input product taken separately while applying a similar radiometric corrections algorithm and transforming the geometry to the same spatial extent (tiles). More precisely, the S10 dataset provides images with the same spatial resolution as the original MSI bands. However, the images are radiometrically corrected with the same LaSRC atmospheric corrections used in Landsat 8. The bands are spectrally adjusted to match the OLI sensor

of Landsat 8. The S30 product is computed from S10 and upscaled to a spatial resolution of 30m. The L30 product is resampled and gridded to the same reference system as S30 to allow pixels to be stacked in time series. This means that the Landsat images are georeferenced on the Sentinel grid. To correct the variations in the images due to the different viewing and illumination angles (resulting from the different flyover time-in-day), both the S30 and L30 products are normalized using the same bidirectional reflectance distribution function (BRDF) calibrated for each sensor to Nadir BRDF-adjusted reflectance (NBAR).

Table 2: HLS data products (Claverie et al., 2018)

	S10	**S30**	**L30**
Spatial	Same as Sentinel-2 L1C	30 m	30 m
Spectral	Same as Sentinel-2 L1C	OLI-like and red-edge bands	OLI and TIRS
Temporal	Same as Sentinel-2 L1C	As input	As input
SR/NBAR	Surface Reflectance	NBAR	NBAR

To minimize differences between Landsat 8 and Sentinel-2 and offer a coherent product with an improved temporal resolution the authors proposed the processing flow presented in Figure 1. First, they apply atmospheric corrections with the Land Surface Reflectance Code algorithm developed for Landsat 8 imagery and extended for Sentinel-2 which accounts for molecular and particle scattering, as well as absorption by ozone and water vapor (Doxani et al., 2018; Vermote et al., 2016). At this step, they also compute the cloud and shadow mask for each product. Secondly, they compute the geometric resampling and geographic registration. This is meant to correct for the misregistrations between images and with the geoid that are already present in the original products and that may account for misregistration of multiple pixels between images (Skakun et al., 2017; Storey et al., 2016; Yan et al., 2018). At this step, S10 is upscaled to a spatial resolution of 30m (→ S30) to match Landsat 8 images so that they can be stacked in a spatially coherent data cube. Thirdly, the S30 and L30 are normalized for per-pixel view and per-tile illumination angles following the method developed by Roy et al. (2016; 2017) that uses a constant BRDF shape and global weights. Finally, the S30 product is spectrally adjusted to minimize the differences between equivalent MSI and OLI bands using a linear regression equation for each band.

The HLS dataset offers a coherent suite of products that have the advantage to be gridded to the same reference system while also being spectrally corrected to be indistinguishable (for L30/S30), hence, allowing to form a data cube with an increased temporal resolution compared to the input products. The downside of this approach is that valuable information – 9 pixels - present in Sentinel-2 imagery is condensed in a single pixel.
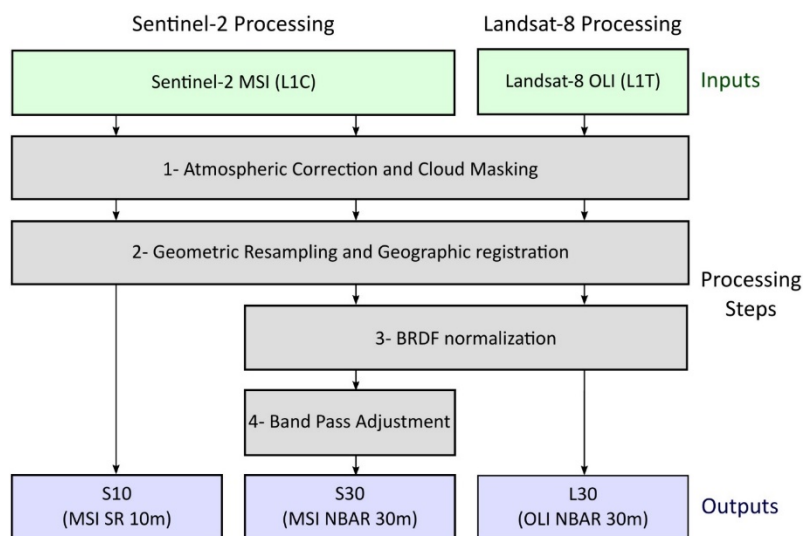

Figure 1: Overview of the HLS processing. The four processing steps are colored in grey (Claverie et al., 2018)

Multiple-point statistics, Direct sampling (Oriani et al., 2021)

The second method was proposed by Oriani et al. (2021) and differs from the previous one as it improves the spatial resolution of the lowest resolution (LR) product to match it of the higher resolution (HR) one. It also converts the spectral characteristics of the LR image to those of the HR image. The method is based on the algorithm of Direct Sampling (DS), a geostatistical simulation technique based on Multiple-Point statistics (MPS).

To demonstrate their method, the author used images from two different sensors. The HR images are composed of 4 bands (R, G, B, NIR) from Worldview-3 and -4 at a resolution of 1.24m. They were used as training images (as a source of high-resolution patterns) and to validate the results. The LR images have a resolution of 3m and are also composed of 4 similar bands and are offered by PlanetLabs Dove constellation. The Dove constellation is composed of hundreds of small satellites and offers a daily temporal resolution. However, due to their small size and low cost of the sensor, the images suffer from some biases (Houborg & McCabe, 2018).

The DS algorithm (Figure 2) works by simulating an image based on the LR image used as an input, a training image (TI) that is composed of an HR and LR image pair as well a k-means classification of the LR TI used as a covariate to inform of the data pattern find in the in proximity to the simulated pixel. The patterns in the TI image should be as similar as possible to the patterns found in the target region of the simulation as the performance of the simulation will decrease for larger dissimilarities.

In more detail, it simulates a random and uninformed pixel of the simulation grid by comparing the N nearest neighbor pixel values to the TI and if the error is lower than a manually set threshold, it adds the value of the pixel to the simulation grid. This is repeated until the full grid is completed. The complete simulation can be done multiple times to propose a set of similarly probable realizations.

An example of the results obtained with this method is presented in Figure 3. We see that the method offers much more spatial heterogeneity compared to the LR images but also compared to the images downscaled with the two methods of bicubic interpolation (HBC and LBC). However, we also see that the DS image seems to
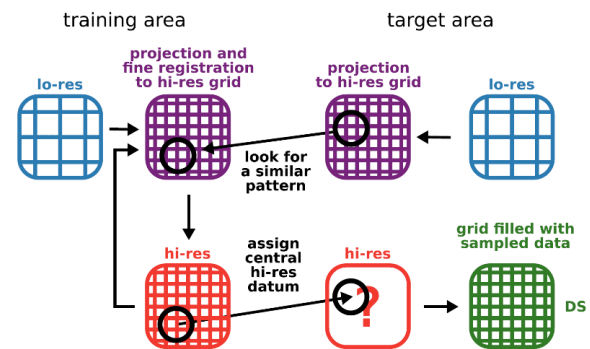

Figure 2: Graphical representation of the DS algorithm. (Oriani et al., 2021)
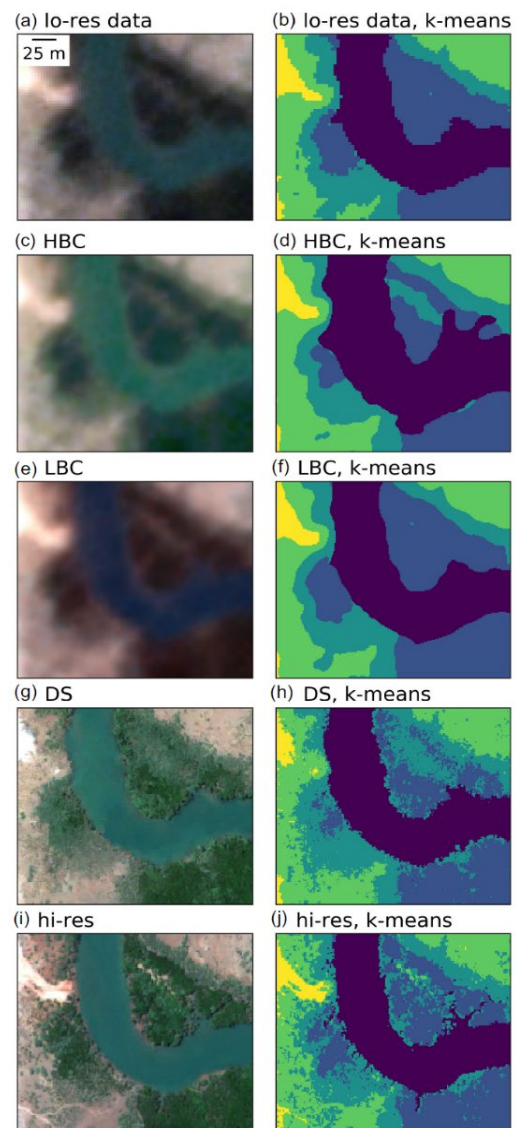

Figure 3: Example of the results of DS compared to two similar methods (HBC, LBC) presented in the article. (Oriani et al., 2021)

have a little less spatial heterogeneity compared to the reference image.

This method offers an improved way to downscaled satellite imagery and could be used at larger scales to provide denser temporal series of a given region with the necessity to obtain only a limited number of TIs. Moreover, it transforms the histogram of the LR image in one similar to the TI and thus would allow treating a time series as if it came from a single sensor. However, the large computing cost compared to other methods might make it more suitable for applications where only a few numbers of images are needed.

ATPRK (Wang et al., 2017)

Wang et al. (2017) proposed an application of area-to-point regression kriging (ATPRK) for the fusion of Landsat 8 and Sentinel-2 images. More precisely, they offer a method to create a coherent dataset of Landsat 8 2-7 bands downscaled to 10m by using Sentinel-2 2, 3, 4, 8, 11, 12 bands. They also downscale the Sentinel-2 11 and 12 bands to 10m (originally 20m) using ATPRK.

ATPRK is a downscaling method consisting of a regression-based trend estimation and area-to-point kriging (ATPK)-based residual prediction. The information in the low-resolution image is used as the primary variable while the information in other bands is used as covariates. The algorithm proposed by the author is cleverly thought as it not only makes full use of the information from the Sentinel-2 images but also the information found in the Landsat 8 panchromatic band that has a resolution of 15m to downscale the 30m bands of Landsat. This has the advantage to consider and correct for possible major changes in the landcover and land use (LCLU) that could have occurred between the Landsat and Sentinel images as the Landsat panchromatic band is taken at the same time as the other bands.

The general workflow is structured as follows (adapted from (Q. Wang et al., 2017)) and is shown in Figure 4:

1) Using ATPRK, the 20m Sentinel-2 bands 11 and 12 are downscaled to 10m using the 10m bands 2, 3, 4, and 8 as covariates.
2) Using ATPRK, the 30m Landsat 8 bands 2-4 are downscaled to 15m using the 15m Landsat 8 panchromatic band as the covariate.
3) Using bicubic interpolation, Sentinel-2 10m bands 2-4 are downscaled to 5m.
4) Using ATPRK, the 15m Landsat 8 bands 2-4 resulting from step 2) are downscaled to 5m. For each band, the Sentinel-2 5m band with a similar wavelength sensitivity obtained at step 3) is used as a single covariate.

Figure 4: General workflow of the ATPRK-based fusion approach for downscaling of Landsat 8 bands 2-7.

5) Using bicubic interpolation, the 5m Landsat 8 results from step 4) are upscaled to 10m to produce the final results for Landsat 8 bands 2-4.
6) Landsat 8 bands 5-7 covariance coefficient (CC) between each other, with Landsat 8 panchromatic band and with Sentinel-2 8, 11, and 12 bands are calculated.
7) For each of Landsat 8 bands 5-7, if the CC between it and the Landsat 8 panchromatic band is higher than the CC between it and the corresponding Sentinel-2 band, the process is similar to
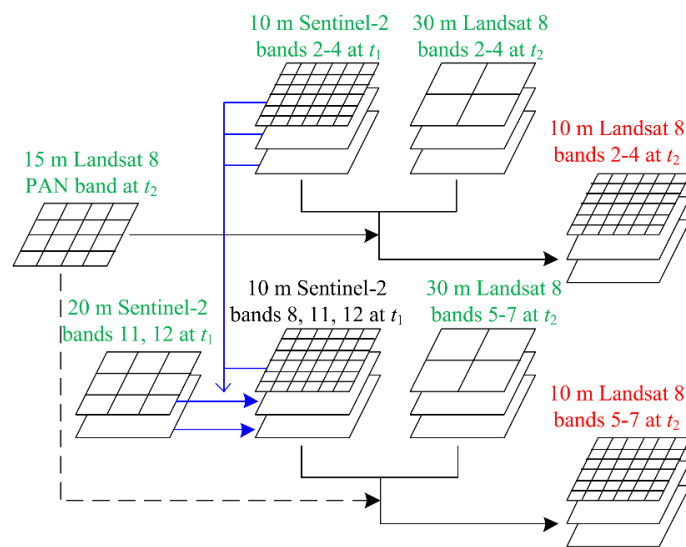
steps 2 to 4 but using Sentinel-2 bands 8, 11 and 12. Otherwise, only the Sentinel-2 band is used as a covariate in the ATPRK.

In this method, the Sentinel-2 bands are used to provide valuable information at the target spatial resolution, while the 15m panchromatic band provides information about potential abrupt changes in LCLU that could have occurred between the Landsat 8 and Sentinel-2 scene. It is worth noting that when little changes in LCLU occurred between the two scenes, using only the Sentinel-2 image as the covariate provides almost the same performance as using both the Sentinel-2 and Landsat panchromatic images as covariates. According to the authors' testing, in most cases using both images provide the best results. Moreover, for the cases where one image alone performs better, using both images only slightly reduces the performance while using the "wrong" image reduces the performance more drastically, meaning that adding bad information has almost no influence on the performance of the downscaling.

The innovative approach to downscaling proposed by the author outperformed STARFM (F. Gao et al., 2006), SFIM (Liu, 2010), and ATWT (Vivone et al., 2014) in every scenario. It provides a way to create a harmonized dataset at the resolution of the Sentinel-2 images, thus not wasting valuable information, while perfectly preserving the spectral proprieties of the Landsat 8 data. The use of both the Sentinel-2 image and the panchromatic band of Landsat 8 allows accounting for LCLU changes.

Deep learning (Shao et al., 2019)

With recent advances in deep learning, new architectures and applications are proposed regularly. Unlike the previous method presented above, artificial neural networks usually require larger training datasets that might be difficult to produce, and the computational time required for their training is comparatively large. However, once trained most neural networks can compute results efficiently. Shao et al. (2019) developed an extended super-resolution convolutional neural network (ESRCNN) for the data fusion of Landsat 8 and Sentinel-2 images. The network is composed of 3 convolutional layers with ReLu as activation function.

The workflow for the fusion of images from the two sensors is presented in Figure 5 and is based on two main phases. In the first phase, the bands 11 and 12 of the Sentinel-2 images are downscaled to 10m by the ESRCNN feeding it with bands 2-4 and 8 at 10m and bands 11 and 12 downscaled at 10m using nearest neighbor (NN) interpolation. The second phase consists of the downscaling of the Landsat 8 bands 1-7 to 10m with ESRCNN by using the panchromatic band, the Sentinel-2 bands 2-4, 8, and 11-12 downscaled at 10m from the previous step, and the Landsat 8 bands 1-7 resampled to 10m using NN interpolation. The second phase is flexible as it can accommodate a different number of Sentinel-2 images as auxiliary data. When no Sentinel-2 image is fed as auxiliary data, the network downsamples the image by only using the 10m downsampled Landsat-8 bands.

The flexibility of the method regarding the number of auxiliary inputs it can accommodate is a good way to maximize the quality of the downscaling when multiple good quality (e.g., low cloud coverage) Sentinel-2 images are available. Indeed, the authors demonstrated that the best performance was obtained with the largest number of Sentinel-2 images as auxiliary data (in this case 3 images) and that the model was able to accommodate images with significant LCLU changes without the creation of artifacts.

The author compared their method to ATPRK, which was the best performing downscaling algorithm at the time, and found that in every scenario ESRCNN outperformed ATPRK. Compared to ESRCNN, ATPRK creates more spectral distortions, especially when sudden changes occur. It also tended to change more the distribution of reflectance value. Moreover, the case with 3 Sentinel-2 images outperformed every other scenario where one or two images were used.
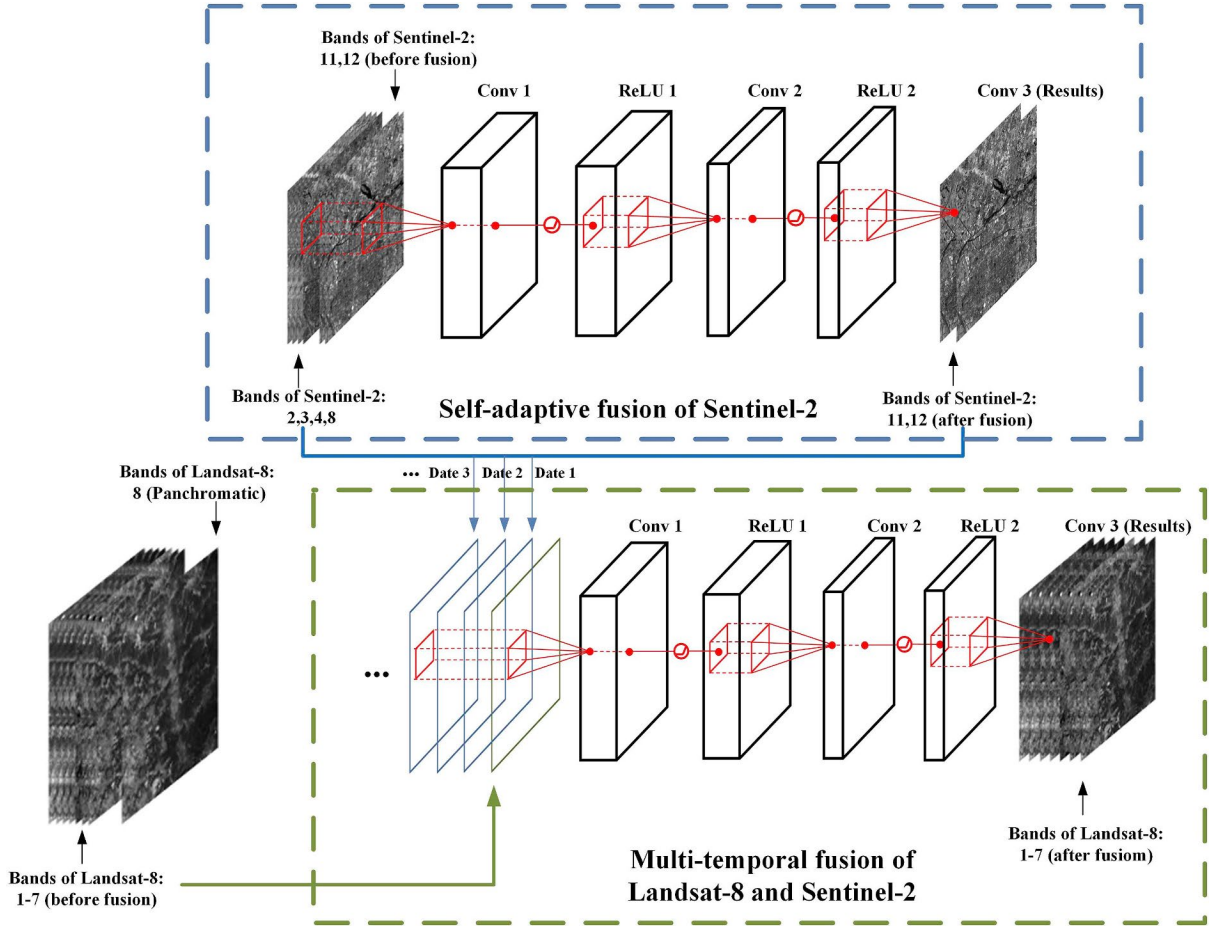
Figure 5: Workflow of ESRCNN for the fusion of Landsat 8 and Sentinel-2 images. (Shao et al., 2019)

ESRCNN offers a well-performing approach for the downscaling of Landsat 8 images and thus for the fusion of the Landsat 8 and Sentinel-2 products. However, compared to other methods like direct sampling or ATPRK, the training of the network is data-hungry, and the creation of an appropriate dataset might prohibitive. Moreover, in the case of this article, the network was trained using upscaled images (90m Landsat 8 and 40m Sentinel-2) so that the original images could be used as reference. This might be problematic as spatial heterogeneity varies at different scales. Additionally, if the method is to be applied to full resolution images, the Landsat 8 images could not be used as the reference, instead, a Sentinel-2 image needs to be used during the training. This implies that the reference image could not be used as input and thus makes the creation of the training dataset even more difficult.

Generative Adversarial networks (Chen et al., 2021)

Generative adversarial networks (GANs) have produced impressive results for the super-resolution of generic images (Ledig et al., 2016) and have thus been applied for the downscaling of satellite images (e.g., Z. Wang et al., 2020). Chen et al. (2021) have proposed a method of downscaling based on a GAN to produce Sentinel-2-like Landsat images by taking advantage of the concurrent observations of Sentinel-2 and Landsat 8. Their goal is to leverage Landsat 8 and Sentinel-2 observations during their overlapping period, from 2016 to 2019, to train a GAN-based model and use it to transform historical Landsat (when no Sentinel-2 data is available) into 10m Sentinel-2-like images.

Generative adversarial networks were introduced in 2014 and consist of two networks, the generator G and the discriminator D, that compete in a game. The goal of G is to produce images that are as similar as possible to the target images to fool D whose goal is to distinguish between true and generated images. Both networks are updated dynamically and results from D are integrated into the loss for G.

For this study, the author collected 11 cloud-free Landsat 8 and Sentinel-2 image pairs from 2016 to 2019. The images were not more than 5 days apart to maximize their similarity. To test the performance of their model on historical images, the authors created a temporal series from Landsat imagery from 1985 to 2018.
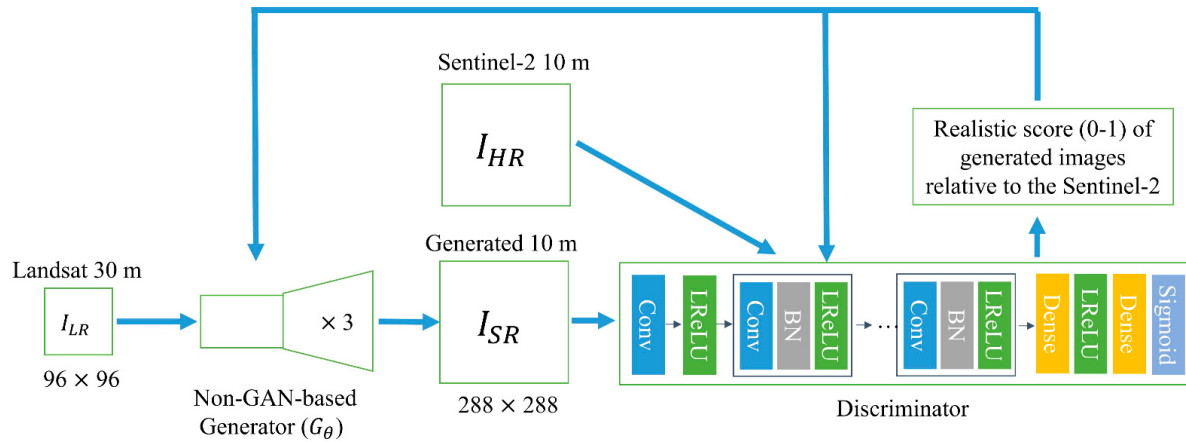

Figure 6: The architecture proposed by (Chen et al., 2021) for the fusion of Landsat and Sentinel-2 imagery.

The architecture of the proposed model is shown in Figure 6. G takes as input a 96x96 pixels patch of Landsat image and downscales it to a patch of 288x288 pixels which is fed to D along with the reference Sentinel-2 patch. D outputs the realistic score of the generated image relatively to the reference image. Then, this score is used to compute the loss of G.

To assess the performance of the GAN-based model, the author compared it with historical methods and a non-GAN-based model. According to their testing, they showed that the non-GAN-based model was better at retaining spectral fidelity while the GAN-based model was able to construct more detailed high-frequency spatial patterns. Moreover, they found that ATPRK achieved a comparable performance in preserving spatial and spectral information. However, ATPRK requires the input of both the low-resolution Landsat image and one or more high-resolution references images. This is not the case for both deep learning-based models, which, once trained do not require reference images. This outlines the potential of deep learning-based methods for the conversion of historical data, where no reference image is available.

According to the authors, the downscaling of historical Landsat imagery produced relatively good results, with no obvious artifact and realistic spectral characteristics and spatial details. These results are encouraging as downscaling and translating Landsat historical data to Sentinel-2-like images would provide a coherent dataset with current sensors for long-term studies. However, referring to the result in Figure 12 in the original article, we can observe small-scale artifacts and noise that look very similar to the results I obtained with the generically trained model. This could be the sign of a model that has not been trained on a large enough dataset, as I could not see similar patterns with the generically trained network in the case of my experiments. This points back to the previously discussed problem of the difficulties in producing a large enough dataset for the training of deep learning-based methods.

Conclusion

In this report, I reviewed five currently used methods for the fusion of satellite imagery. Two main approaches are currently used, the easiest method is to upscale the high-resolution imagery to match it of the lowest resolution one. However, this is wasteful and new methods that downscale the low-resolution product have been developed and tested. The problem with those methods is that they need temporally close images from both sensors and thus could not be used without modifications to match sensors from different periods. The exception being GAN-based methods that could be trained on

contemporary images to learn the characteristic of a Sentinel-2 like images and generate such images from older sources.

The HLS2 data set is the one initiative that offers a finalized dataset that can be directly used by the scientific community, though the spatial resolution of the Sentinel-2 images is lost. It might however be well suited for some applications and simplify the work of researchers.

Direct sampling and ATPRK seem to be well suited for small-scale downscaling since they are easy to implement once the reference image for DS and the collocated images for ATPRK are found. On the other end, deep learning-based methods are more tedious to train but offer an efficient way to produce large quantities once the training phase is completed.

It could be interesting to produce an enhanced HLS2 by using the already computed S10 and L30 products (that are already perfectly gridded) and, using a GAN-based model, generate the L10 data product. This would probably allow creating an even more coherent dataset L10/S10 and L30/S30 images that could be used seamlessly depending on the demands of the application.

References

Chen, B., Li, J., & Jin, Y. (2021). Deep learning for feature-level data fusion: Higher resolution reconstruction of historical landsat archive. *Remote Sensing*, *13*(2), 1–23. https://doi.org/10.3390/rs13020167

Claverie, M., Demarez, V., Duchemin, B., Hagolle, O., Ducrot, D., Marais-Sicre, C., Dejoux, J. F., Huc, M., Keravec, P., Béziat, P., Fieuzal, R., Ceschia, E., & Dedieu, G. (2012). Maize and sunflower biomass estimation in southwest France using high spatial and temporal resolution remote sensing data. *Remote Sensing of Environment*, *124*, 844–857. https://doi.org/10.1016/j.rse.2012.04.005

Claverie, M., Ju, J., Masek, J. G., Dungan, J. L., Vermote, E. F., Roger, J. C., Skakun, S. V., & Justice, C. (2018). The Harmonized Landsat and Sentinel-2 surface reflectance data set. *Remote Sensing of Environment*, *219*(August), 145–161. https://doi.org/10.1016/j.rse.2018.09.002

DeVries, B., Decuyper, M., Verbesselt, J., Zeileis, A., Herold, M., & Joseph, S. (2015). Tracking disturbance-regrowth dynamics in tropical forests using structural change detection and Landsat time series. *Remote Sensing of Environment*, *169*, 320–334. https://doi.org/10.1016/j.rse.2015.08.020

Doxani, G., Vermote, E., Roger, J. C., Gascon, F., Adriaensen, S., Frantz, D., Hagolle, O., Hollstein, A., Kirches, G., Li, F., Louis, J., Mangin, A., Pahlevan, N., Pflug, B., & Vanhellemont, Q. (2018). Atmospheric correction inter-comparison exercise. *Remote Sensing*, *10*(2), 1–18. https://doi.org/10.3390/rs10020352

Gao, F., Masek, J., Schwaller, M., & Hall, F. (2006). On the blending of the landsat and MODIS surface reflectance: Predicting daily landsat surface reflectance. *IEEE Transactions on Geoscience and Remote Sensing*, *44*(8), 2207–2218. https://doi.org/10.1109/TGRS.2006.872081

Gao, S., Niu, Z., Huang, N., & Hou, X. (2013). Estimating the Leaf Area Index, height and biomass of maize using HJ-1 and RADARSAT-2. *International Journal of Applied Earth Observation and Geoinformation*, *24*(1), 1–8. https://doi.org/10.1016/j.jag.2013.02.002

Hansen, M. C., & Loveland, T. R. (2012). A review of large area monitoring of land cover change using Landsat data. *Remote Sensing of Environment*, *122*, 66–74. https://doi.org/10.1016/j.rse.2011.08.024

Hölbling, D., Abad, L., Dabiri, Z., Prasicek, G., Tsai, T. T., & Argentin, A. L. (2020). Mapping and analyzing the evolution of the butangbunasi landslide using landsat time series with respect to heavy rainfall events during typhoons. *Applied Sciences (Switzerland)*, *10*(2), 1–21. https://doi.org/10.3390/app10020630

Houborg, R., & McCabe, M. F. (2018). Daily retrieval of NDVI and LAI at 3 m resolution via the fusion of CubeSat, Landsat, and MODIS data. *Remote Sensing*, *10*(6). https://doi.org/10.3390/rs10060890

Ledig, C., Theis, L., Huszar, F., Caballero, J., Cunningham, A., Acosta, A., Aitken, A., Tejani, A., Totz, J., Wang, Z., & Shi, W. (2016). Photo-Realistic Single Image Super-Resolution Using a Generative Adversarial Network. *Proceedings - 30th IEEE Conference on Computer Vision and Pattern Recognition, CVPR 2017*, *2017-January*, 105–114. http://arxiv.org/abs/1609.04802

Li, J., & Chen, B. (2020). Global Revisit Interval Analysis of Landsat-8 -9 and Sentinel-2A -2B Data for Terrestrial Monitoring. *Sensors (Basel, Switzerland)*, *20*(22), 1–15. https://doi.org/10.3390/S20226631

Li, J., & Roy, D. P. (2017). A global analysis of Sentinel-2a, Sentinel-2b and Landsat-8 data revisit intervals and implications for terrestrial monitoring. *Remote Sensing*, *9*(9). https://doi.org/10.3390/rs9090902

Liu, J. G. (2010). Smoothing Filter-based Intensity Modulation: A spectral preserve image fusion technique for improving spatial details. *Http://Dx.Doi.Org/10.1080/014311600750037499*, *21*(18), 3461–3472. https://doi.org/10.1080/014311600750037499

Loveland, T. R., & Dwyer, J. L. (2012). Landsat: Building a strong future. *Remote Sensing of Environment*, *122*, 22–29. https://doi.org/10.1016/J.RSE.2011.09.022

Ma, H., Huang, J., Zhu, D., Liu, J., Su, W., Zhang, C., & Fan, J. (2013). Estimating regional winter wheat yield by assimilation of time series of HJ-1 CCD NDVI into WOFOST-ACRM model with Ensemble Kalman Filter. *Mathematical and Computer Modelling*, *58*(3–4), 759–770. https://doi.org/10.1016/j.mcm.2012.12.028

Melaas, E. K., Friedl, M. A., & Zhu, Z. (2013). Detecting interannual variation in deciduous broadleaf forest phenology using Landsat TM/ETM+ data. *Remote Sensing of Environment*, *132*, 176–185. https://doi.org/10.1016/j.rse.2013.01.011

Oriani, F., McCabe, M. F., & Mariethoz, G. (2021). Downscaling Multispectral Satellite Images without Colocated High-Resolution Data: A Stochastic Approach Based on Training Images. *IEEE Transactions on Geoscience and Remote Sensing*, *59*(4), 3209–3225. https://doi.org/10.1109/TGRS.2020.3008015

Ranghetti, L., Boschetti, M., Nutini, F., & Busetto, L. (2020). "sen2r": An R toolbox for automatically downloading and preprocessing Sentinel-2 satellite data. *Computers and Geosciences*, *139*(May 2019). https://doi.org/10.1016/j.cageo.2020.104473

Roy, D. P., Zhang, H. K., Ju, J., Gomez-Dans, J. L., Lewis, P. E., Schaaf, C. B., Sun, Q., Li, J., Huang, H., & Kovalskyy, V. (2016). A general method to normalize Landsat reflectance data to nadir BRDF adjusted reflectance. *Remote Sensing of Environment*, *176*, 255–271. https://doi.org/10.1016/j.rse.2016.01.023

Roy, David P., Li, J., Zhang, H. K., Yan, L., Huang, H., & Li, Z. (2017). Examination of Sentinel-2A multi-spectral instrument (MSI) reflectance anisotropy and the suitability of a general method to normalize MSI reflectance to nadir BRDF adjusted reflectance. *Remote Sensing of Environment*, *199*, 25–38. https://doi.org/10.1016/j.rse.2017.06.019

Shao, Z., Cai, J., Fu, P., Hu, L., & Liu, T. (2019). Deep learning-based fusion of Landsat-8 and Sentinel-2 images for a harmonized surface reflectance product. *Remote Sensing of Environment*, *235*(June), 111425. https://doi.org/10.1016/j.rse.2019.111425

Sibanda, M., Mutanga, O., & Rouget, M. (2015). Examining the potential of Sentinel-2 MSI spectral resolution in quantifying above ground biomass across different fertilizer treatments. *ISPRS Journal of Photogrammetry and Remote Sensing*, *110*, 55–65.

https://doi.org/10.1016/j.isprsjprs.2015.10.005

Skakun, S., Kussul, N., Shelestov, A., & Kussul, O. (2014). Flood Hazard and Flood Risk Assessment Using a Time Series of Satellite Images: A Case Study in Namibia. *Risk Analysis*, *34*(8), 1521–1537. https://doi.org/10.1111/risa.12156

Skakun, S., Vermote, E., Roger, J.-C., & Franch, B. (2017). Combined Use of Landsat-8 and Sentinel-2A Images for Winter Crop Mapping and Winter Wheat Yield Assessment at Regional Scale. *AIMS Geosciences*, *3*(2), 163–186. https://doi.org/10.3934/geosci.2017.2.163

Storey, J., Roy, D. P., Masek, J., Gascon, F., Dwyer, J., & Choate, M. (2016). A note on the temporary misregistration of Landsat-8 Operational Land Imager (OLI) and Sentinel-2 Multi Spectral Instrument (MSI) imagery. *Remote Sensing of Environment*, *186*(2016), 121–122. https://doi.org/10.1016/j.rse.2016.08.025

U.S. Geological Survey. (2016). Landsat 8 Data Users Handbook. *Nasa*, *8*(June), 97. https://landsat.usgs.gov/documents/Landsat8DataUsersHandbook.pdf

Vermote, E., Justice, C., Claverie, M., & Franch, B. (2016). Preliminary analysis of the performance of the Landsat 8/OLI land surface reflectance product. *Remote Sensing of Environment*, *185*, 46–56. https://doi.org/10.1016/j.rse.2016.04.008

Vivone, G., Restaino, R., Mura, M. D., Licciardi, G., & Chanussot, J. (2014). Contrast and error-based fusion schemes for multispectral image pansharpening. *IEEE Geoscience and Remote Sensing Letters*, *11*(5), 930–934. https://doi.org/10.1109/LGRS.2013.2281996

Vrieling, A., Skidmore, A. K., Wang, T., Meroni, M., Ens, B. J., Oosterbeek, K., O'Connor, B., Darvishzadeh, R., Heurich, M., Shepherd, A., & Paganini, M. (2017). Spatially detailed retrievals of spring phenology from single-season high-resolution image time series. *International Journal of Applied Earth Observation and Geoinformation*, *59*, 19–30. https://doi.org/10.1016/j.jag.2017.02.021

Wang, Q., Blackburn, G. A., Onojeghuo, A. O., Dash, J., Zhou, L., Zhang, Y., & Atkinson, P. M. (2017). Fusion of Landsat 8 OLI and Sentinel-2 MSI Data. *IEEE Transactions on Geoscience and Remote Sensing*, *55*(7), 3885–3899. https://doi.org/10.1109/TGRS.2017.2683444

Wang, Z., Jiang, K., Yi, P., Han, Z., & He, Z. (2020). Ultra-dense GAN for satellite imagery super-resolution. *Neurocomputing*, *398*, 328–337. https://doi.org/10.1016/j.neucom.2019.03.106

Whitcraft, A. K., Becker-Reshef, I., & Justice, C. O. (2015). A framework for defining spatially explicit earth observation requirements for a global agricultural monitoring initiative (GEOGLAM). *Remote Sensing*, *7*(2), 1461–1481. https://doi.org/10.3390/rs70201461

Yan, L., Roy, D. P., Li, Z., Zhang, H. K., & Huang, H. (2018). Sentinel-2A multi-temporal misregistration characterization and an orbit-based sub-pixel registration methodology. *Remote Sensing of Environment*, *215*(September 2017), 495–506. https://doi.org/10.1016/j.rse.2018.04.021

Zhu, Z., Woodcock, C. E., & Olofsson, P. (2012). Continuous monitoring of forest disturbance using all available Landsat imagery. *Remote Sensing of Environment*, *122*, 75–91. https://doi.org/10.1016/j.rse.2011.10.030